

9-26-2022

Model-based determination of the synchronization delay between MRI and trajectory data.

Paul Ioan Dubovan

Corey Allan Baron

Follow this and additional works at: <https://ir.lib.uwo.ca/robarthpub>



Part of the [Bioimaging and Biomedical Optics Commons](#)

Citation of this paper:

Dubovan, Paul Ioan and Baron, Corey Allan, "Model-based determination of the synchronization delay between MRI and trajectory data." (2022). *Robarts Imaging Publications*. 29.
<https://ir.lib.uwo.ca/robarthpub/29>

TECHNICAL NOTE

Model-based determination of the synchronization delay between MRI and trajectory data

Paul Ioan Dubovan^{1,2} | Corey Allan Baron^{1,2}  

¹Department of Medical Biophysics, Western University, London, Ontario Canada

²Center for Functional and Metabolic Mapping, Western University, London, Ontario Canada

Correspondence

Corey Allan Baron, Department of Medical Biophysics, Western University, London, Ontario, Canada.

Email: corey.baron@uwo.ca

Funding information

Canada First Research Excellence Fund, Grant/Award Number: BrainsCAN; Natural Sciences and Engineering Research Council of Canada, Grant/Award Number: PGS-D; Natural Sciences and Engineering Research Council of Canada (NSERC), Grant/Award Number: RGPIN-2018-05448; Ontario Graduate Scholarship program; Canada Foundation for Innovation

Purpose: Real-time monitoring of dynamic magnetic fields has recently become a commercially available option for measuring MRI k-space trajectories and magnetic fields induced by eddy currents in real time. However, for accurate image reconstructions, sub-microsecond synchronization between the MRI data and field dynamics (ie, k-space trajectory plus other spatially varying fields) is required. In this work, we introduce a new model-based algorithm to automatically perform this synchronization using only the MRI data and field dynamics.

Methods: The algorithm works by enforcing consistency among the MRI data, field dynamics, and receiver sensitivity profiles by iteratively alternating between convex optimizations for (a) the image and (b) the synchronization delay. A healthy human subject was scanned at 7 T using a transmit-receive coil with integrated field probes using both single-shot spiral and EPI, and reconstructions with various synchronization delays were compared with the result of the proposed algorithm. The accuracy of the algorithm was also investigated using simulations, in which the acquisition delays for simulated acquisitions were determined using the proposed algorithm and compared with the known ground truth.

Results: In the in vivo scans, the proposed algorithm minimized artifacts related to synchronization delay for both spiral and EPI acquisitions, and the computation time required was less than 30 s. The simulations demonstrated accuracy to within tens of nanoseconds.

Conclusions: The proposed algorithm can automatically determine synchronization delays between MRI data and field dynamics measured using a field probe system.

KEYWORDS

delay, eddy currents, field monitoring, field probes, model-based, non-Cartesian, synchronization

1 | INTRODUCTION

Non-Cartesian MRI provides the advantages of increased SNR due to shortened TEs, robustness to motion, and more time-efficient data acquisition. However, non-Cartesian approaches are generally more sensitive to k-space errors from eddy currents compared with Cartesian sampling, which ultimately results in blurring and/or geometric distortions. Many approaches to estimate these k-space errors have been proposed, which include direct measurement of the trajectory,¹⁻³ calibration based on a gradient impulse response function,^{4,5} or via retrospective modeling.⁶ Alternatively, real-time monitoring using field probes has recently become a commercially available rapid option for measuring k-space trajectories and eddy current fields in real time, up to second or third order in space.⁷⁻¹⁰ These measured field dynamics can be included together with an off-resonance map in an expanded encoding model based reconstruction that greatly ameliorates artifacts from off-resonance and eddy currents.⁷ However, due to hardware-specific filter delays that differ between the MRI and field-probe spectrometers and transit time for the trigger pulse that initiates field probe measurements, the relative timing between the field-probe measured field dynamics and the MRI signal is unknown and may vary on the order of 1 μ s between scans. An error in this timing, which leads to image artifacts, will henceforth be referred to as a “synchronization delay.”

Gradient delays and their associated artifacts have been well-described for non-Cartesian acquisitions that do not use external field monitoring, where there are generally separate delays for each of the three gradient channels instead of the single global synchronization delay that is required to be determined for field-monitored acquisitions. Various approaches for correcting for these delays have been proposed, which include pulse-sequence modifications or a separate calibration scan¹¹⁻¹³ and retrospective methods that are designed for particular trajectories.^{11,14-17} While these methods could likely be adapted to determine the synchronization delay required for acquisitions using field monitoring, the necessity for either specific pulse-sequence prescans or specific trajectories creates a complicated solution landscape with various trade-offs, depending on the approach. A promising self-consistency approach that explicitly determines delays has been proposed, in which gradient delays and receiver sensitivity profiles are simultaneously estimated from fully sampled calibration data using low-rank constraints,¹⁸ but this method is not applicable for situations in which the receiver-sensitivity calibration data are obtained from a separate scan, as is typically the case for reconstructions using field-probe measurements.

In this work, we introduce a general model-based retrospective approach to determine the synchronization delay between measured field dynamics and the MRI data that is applicable to arbitrary trajectories and require no pulse-sequence modification. Furthermore, we demonstrate that it can accurately estimate the delay even when aggressive coil compression is used and propose an approach to greatly accelerate convergence, making this method require very little time for computations. We demonstrate the performance of the algorithm for both single-shot spiral and EPI acquisitions in the brain of a healthy human subject and through simulation.

2 | THEORY

The signal y_m^j measured at time t_m by receiver element j originates from a range of locations r_n and can be modeled using^{7,9}

$$y_m^j = \sum_n C^j(r_n) x(r_n) e^{i\omega(r_n)t_m} e^{i\sum_l k_l(t_m+\tau+\Delta\tau)b_l(r_n)}, \quad (1)$$

where C^j is the j th receiver sensitivity profile; x is the image; k_l are the coefficients measured by a field probe system (ie, the “field dynamics,” which include the normal definition of the k-space trajectory, zeroth-order main field fluctuations, and higher spatial orders of fields from eddy currents) for spherical harmonic basis functions b_l (l indexes the different spherical harmonic terms); ω is the off-resonance from B_0 inhomogeneity (measured in a separate scan); τ is the presumed synchronization delay of the MRI signal y relative to $k_l(t)$; and $\Delta\tau$ is the unknown error in τ . The value of τ might be initially estimated based on typical trigger delays or the time for the gradient prephasers required for some trajectories (eg, EPI), for example, and the purpose of this algorithm is to determine the net error-free delay, $\tau + \Delta\tau$. To cast Equation 1 into a form that enables a convex estimation of $\Delta\tau$, we first recognize that for typical delay errors that are on the order of microseconds, $k_l(t_m)$ is approximately linear in the vicinity of each sample m . This approximation allows the substitution $k_l(t_m + \tau + \Delta\tau) = k_l(t_m + \tau) + \Delta\tau k'_l(t_m + \tau)$ where $k'_l(t) = dk_l(t)/dt$, yielding

$$y_m^j = \sum_n C^j(r_n) x(r_n) e^{i\omega(r_n)t_m} e^{i\sum_l k_l(t_m+\tau)b_l(r_n)} e^{i\Delta\tau \sum_l k'_l(t_m+\tau)b_l(r_n)}. \quad (2)$$

Furthermore, for small $\Delta\tau$, the net phase $\Delta\tau \sum_l k'_l(t_m + \tau) b_l(r_n) \ll 1$, allowing the use of a Taylor approximation $e^{i\Delta\tau \sum_l k'_l(t_m+\tau)b_l(r_n)} \approx 1 + i\Delta\tau \sum_l k'_l(t_m + \tau) b_l(r_n)$, yields the following:

TABLE 1 Algorithm for the joint optimization of τ and x , "Algorithm 1"

Input: $\Delta\tau_{min}, \tau_0, \gamma_0$
Output: τ, x
Initialization: $\Delta\tau_0 = \infty, p = 0$
1: while $\Delta\tau_p > \Delta\tau_{min}$ do
2: $p = p + 1$
3: interpolate $k_l(t)$ and $k'_l(t)$ to time samples $t_m + \tau_{p-1}$, and form A_p and B_p
4: $x_p = \operatorname{argmin}_x \ A_p x - Y\ _2^2$
5: $\Delta\tau_p = \operatorname{Re} \left[\left((B_p x_p)^H (B_p x_p) \right)^{-1} (B_p x_p)^H (Y - A_p x_p) \right]$
6: if $p > 1$ and $\operatorname{sign}(\Delta\tau_p) \neq \operatorname{sign}(\Delta\tau_{p-1})$ then
7: $\gamma_p = \max(1, \gamma_{p-1}/2)$
8: else
9: $\gamma_p = \gamma_{p-1}$
10: end if
11: $\tau_p = \tau_{p-1} + \gamma_p \Delta\tau$
12: end while
13: return τ_p, x_p

$$y_m^j = \sum_n C^j(r_n) x(r_n) e^{i\omega(r_n)t_m} e^{i \sum_l k_l(t_m+\tau) b_l(r_n)} + \Delta\tau i \sum_n \sum_l k'_l(t_m + \tau) b_l(r_n) C^j(r_n) x(r_n) e^{i\omega(r_n)t_m} e^{i \sum_l k_l(t_m+\tau) b_l(r_n)}.$$

Equation 3 can be cast into a matrix equation over all receivers as follows:

$$\begin{aligned} \Delta\tau Bx &= Y - Ax \\ Y_{m+jN_s} &= Y_m^j \\ A_{m+jN_s, n} &= C^j(r_n) e^{i\omega(r_n)t_m} e^{i \sum_l k_l(t_m+\tau) b_l(r_n)} \\ B_{m+jN_s, n} &= i \sum_l k'_l(t_m + \tau) b_l(r_n) C^j(r_n) e^{i\omega(r_n)t_m} e^{i \sum_l k_l(t_m+\tau) b_l(r_n)} \end{aligned} \quad (4)$$

where N_s is the number of samples acquired. If N_r is the number of receivers and N_x is the number of object-domain voxels in x , then A and B are matrices of size $N_s N_r$ by N_x . Accordingly, Bx and $Y - Ax$ are each column vectors with length equal to $N_s N_r$, and $\Delta\tau$ can be determined in a least-squares sense via

$$\Delta\tau = \operatorname{Re} \left[\left((Bx)^H (Bx) \right)^{-1} (Bx)^H (Y - Ax) \right]. \quad (5)$$

The determination of $\Delta\tau$ requires knowledge of the image x . Accordingly, we jointly solve for x and $\Delta\tau$ by iteratively alternating between determining x at iteration p using

$$x_p = \operatorname{argmin}_x \|A_p x - Y\|_2^2, \quad (6)$$

and solving for $\Delta\tau$ using direct matrix implementation of Equation 5. Equation 6 is solved using the conjugate gradient method. For every iteration, p , $k_l(t_m + \tau_p)$ is re-interpolated from the original field probe samples via $\tau_p = \tau_{p-1} + \Delta\tau_{p-1}$. Likewise, $k'_l(t)$ is estimated

using a 5-point central difference of the field probe data that is then interpolated to the MRI samples located at $t_m + \tau_p$. All interpolations used piecewise cubic Hermite interpolation.¹⁹ Iterations continue until $\Delta\tau_p$ is less than a user-specified threshold, $\Delta\tau_{min}$. The net algorithm, Algorithm 1, is found in Table 1. Notably, this joint optimization is only required for a single sample slice because the delay is not expected to change for different slices.

In practice, Algorithm 1 may converge slowly. To accelerate convergence, we propose to scale $\Delta\tau_p$ by a factor γ in every iteration. If the polarity of $\Delta\tau_p$ changes from one iteration to the next, it suggests that γ is too large; thus, γ is reduced by a factor of 2 for the next iteration, subject to $\gamma \geq 1$. Coil compression performs a compression of the receiver channels into fewer virtual channels using a linear transformation determined from singular value decomposition, which can drastically reduce memory requirements and accelerate image reconstructions.^{20–23} Accordingly, in this work the impact of coil compression on the accuracy of Algorithm 1 will also be evaluated by varying the number of virtual coils, N_r .

3 | METHODS

3.1 | Data acquisition and reconstruction parameters

A healthy patient was scanned on a 7T head-only MRI (Siemens MAGNETOM Terra Plus) at Western University's Center for Functional and Metabolic Mapping

(80-mT/m gradient strength and 400-T/m/s max slew rate), which was approved by the institutional review board at Western University, and informed consent was obtained before scanning. The scans used a 32-channel receive coil with integrated field probes.²⁴ A single-shot spiral acquisition was performed with an in-plane resolution of $1.5 \times 1.5 \text{ mm}^2$, 3-mm slice thickness (10 slices), TE/TR = 33/2500 ms, FOV = $192 \times 192 \text{ mm}^2$, an undersampling rate of 4, dwell time between samples of 2.5 μs , and a total readout time of 13.2 ms. A single-shot spin-echo EPI acquisition was acquired in a separate scanning session with an in-plane resolution of 2 mm^2 , 3-mm slice thickness (10 slices), TE/TR = 59/2500 ms, FOV = $192 \times 192 \text{ mm}^2$, an undersampling rate of 3, dwell time between samples of 2.4 μs , and a total readout time of 16.9 ms. Noise correlation between receivers was corrected using prewhitening before any reconstructions,²⁵ and the data-based method of Zhang et al was used for coil compression.²³ The B_0 field maps were acquired at the same resolution as the single-shot spiral scan using Cartesian-sampled dual-echo gradient echo with TE values of 4.08 and 5.10 ms. The first echo of the same data was used to estimate C^j via ESPiRiT.²⁶ The spatially varying field dynamics up to second order in space were measured simultaneously with the MRI data using a field-monitoring system (Skopec Clip-on Camera) consisting of 16 transmit/receive 19F field probes and a sampling dwell time of 1 μs .²⁴ In all implementations of Algorithm 1, iterations in p were stopped when $\Delta\tau < 0.005 \mu\text{s}$. The object domain support (ie, the FOV images that were reconstructed in Equation 6) was determined by thresholding the B_0 mapping images, which optimizes reconstruction time.²⁷

The initial guess for the synchronization delay was set to 45 μs for spiral acquisitions, which includes hard-coded time allowance for trigger pulse transmission and the field probe excitation pulses. Moreover, we have developed a simple algorithm to determine the starting guess for EPI. In short, this method consists of (a) numerically finding the first zero crossing of the first-order field probe profile that corresponds to the readout gradient, and then (b) subtracting half the duration for reading out a single line of k-space (available from the raw MRI data header) from the position of the zero-crossing.

3.2 | Convergence and coil-compression performance

To investigate the speed increases for $\gamma_0 > 1$, the number of iterations required to determine τ was measured for three cases corresponding to $\gamma_0 = \{1, 3, 10\}$ using the in vivo acquisitions. To investigate the performance of the

algorithm with coil compression, τ was estimated with the full complement of 32 channels as well as 16, 10, and 6 virtual channels ($\gamma_0 = 3$ for all cases).

3.3 | Validation of accuracy

Simulations to validate accuracy were performed by sampling the image acquired in the B_0 mapping scan (after interpolating to the FOV and resolution of the field-monitored scan via modified Akima cubic Hermite interpolation¹⁹) using the forward model defined by Equation 1 with the k_l measured via the field monitoring system. Various choices of τ ranging from $-2.5 \mu\text{s}$ to $2.5 \mu\text{s}$ were simulated for both the spiral and EPI acquisitions described previously. Gaussian white noise (SNR ~ 10 in white matter) was added to the simulated k-space data before using Algorithm 1.

4 | RESULTS

The field dynamics measured using the field probe system for both spiral and EPI are displayed in Figure 1, where

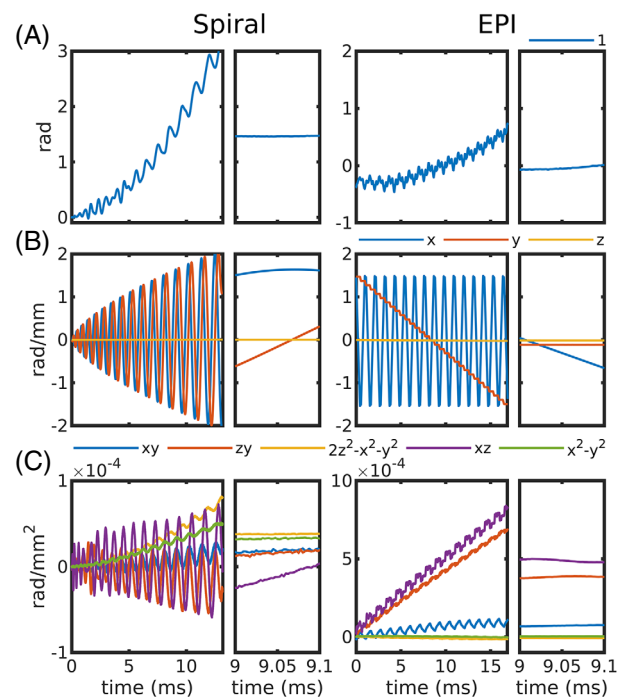
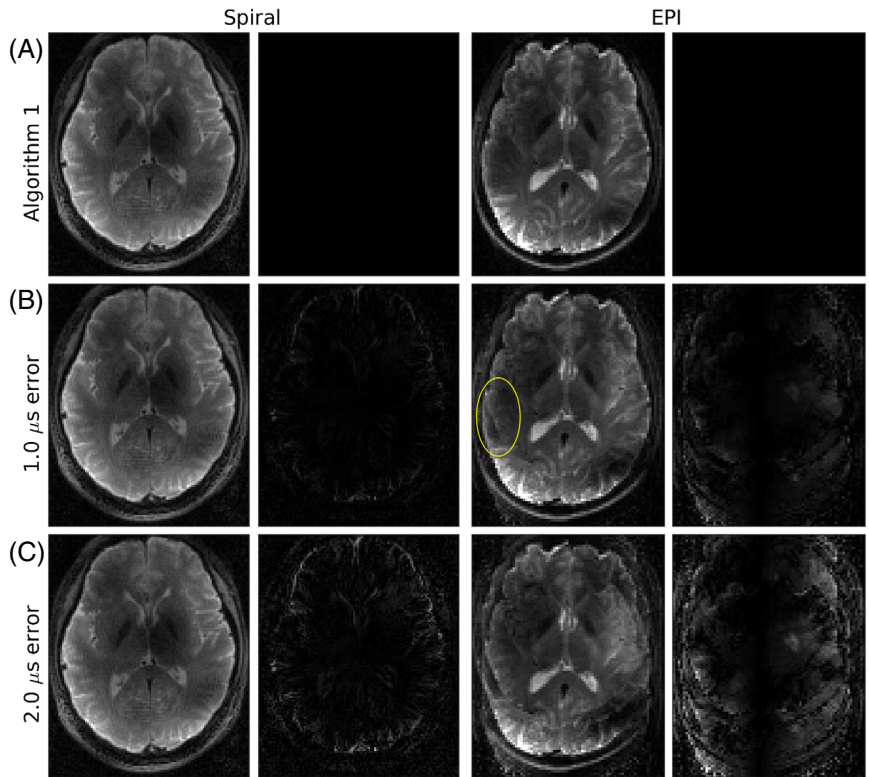


FIGURE 1 Field dynamics measured using the field probe system displayed as the coefficients, $k_l(t)$, corresponding to zeroth (A), first (B), and second (C) order spherical harmonics for each of the spiral and EPI trajectories. The zoomed-in section highlights a 100- μs span of time during which little variation in fields is observed. The basis functions corresponding to each index l are shown above each row of plots

FIGURE 2 A, Image reconstructions that result from Algorithm 1 from both spiral and EPI acquisitions. B,C, The solution of Equation 6 when τ is offset from the result in (A) by $1\ \mu\text{s}$ and $2\ \mu\text{s}$, respectively. The right column for each readout type shows the difference relative to the result of Algorithm 1, scaled by a factor of 2. While spiral exhibits blurring due to delay errors, EPI shows moderate ghosting artifacts for $1\ \mu\text{s}$ of synchronization error (eg, circled) and complete reconstruction failure for an error of $2\ \mu\text{s}$. Similar results are observed in other slices



it is observed that the assumption of slowly varying field changes is valid on time scales of tens to hundreds of μs .

The in vivo images reconstructed from the proposed algorithm show good quality at the automatically determined value of τ (Figure 2A). Substantial artifacts are introduced for EPI when errors in delay are present, while blurring is observed for spiral (Figure 2B,C). The SD of synchronization delays determined from Algorithm 1 across all 10 slices was 34 ns for spiral and 53 ns for EPI.

When $\gamma = 1$, a monotonic convergence of τ is observed, which is greatly accelerated with $\gamma = 3$ (Figure 3A). When the initial γ is chosen to be much too large at a value of 10, the convergence is oscillatory, but still faster than when $\gamma = 1$. When coil compression is used to determine τ for the in vivo scans, there is negligible degradation in accuracy (Figure 3B).

Noise was added to the simulated image reconstructions for both spiral and EPI trajectories to achieve an SNR of approximately 10 in white matter (Supporting Information Figure S1). Highly accurate determination of τ is observed for as low as 10 virtual coils for both spiral and EPI (Figure 4A). For six virtual coils, a small positive bias in τ was observed.

The loss function $\|A_p x - Y\|_2^2$ is shown for a range of starting guesses of τ in Figure 4B. A local minimum is observed for the EPI trajectory for extremely large disparity in the starting guess from the true value, which causes Algorithm 1 to fail in the proximity of the local minimum.

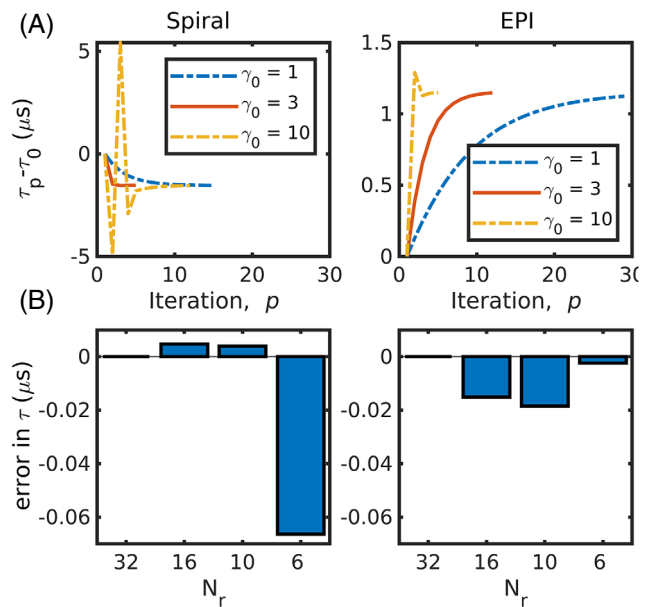


FIGURE 3 A, Convergence of τ for various choices of γ_0 , where p is the iteration number and τ_0 is the initial guess, for both spiral and EPI prospective scans (results from the same slices shown in Figure 2A). B, Error in τ determined from Algorithm 1 as the number of virtual coils used in coil compression is decreased from the full number of 32 coils, where the result from 32 coils is used as the reference. For both spiral and EPI, negligible error is observed for as few as six virtual coils ($< 100\ \text{ns}$). Similar results are observed in other slices

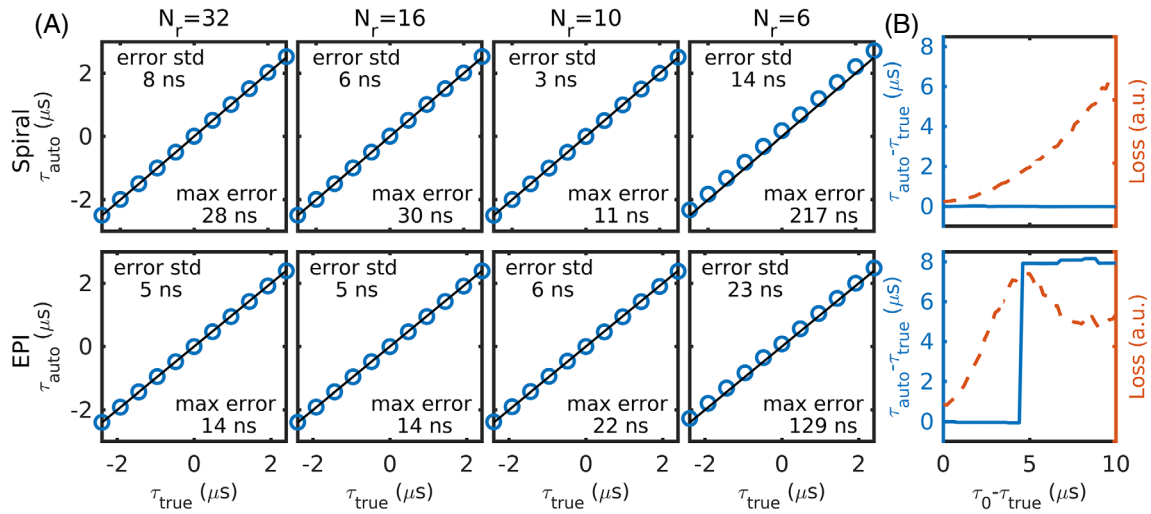


FIGURE 4 Simulations when various synchronization delays (τ_{true}) are used to simulate data sampling via Equation 1. After sampling, noise is added to the simulated signal data ($\text{SNR} \sim 10$) and Algorithm 1 is used to estimate the delay, τ_{auto} . A, Performance of Algorithm 1 for differing numbers of virtual coils (N_r) used in coil compression (initial guess $\tau_0 = 0 \mu\text{s}$, std = standard deviation of $\tau_{\text{auto}} - \tau_{\text{true}}$). The solid line depicts where $\tau_{\text{auto}} = \tau_{\text{true}}$. Example images from the simulations are shown in Supporting Information Figure S1. B, Loss function (red dashed, right vertical axis) and the result of Algorithm 1 (blue solid, left vertical axis), where τ_0 is the initial guess used in Algorithm 1. The loss function was computed as $\|Ax - Y\|_2^2$, where A used $\tau = \tau_0$ (see Equation 4) and x was found via Equation 6 assuming $\tau = \tau_0$. While the shown plot used $\tau_{\text{true}} = 0 \mu\text{s}$, similar results were obtained for other choices of τ_{true} . For an initial guess of the synchronization delay more than $5 \mu\text{s}$ from the true value, Algorithm 1 is attracted to a local minimum for EPI

5 | DISCUSSION

In this work, we have developed a new algorithm for the accurate and rapid determination of the delay between MRI data samples and field dynamics. While we demonstrated the algorithm using data from NMR field probes, it is generalizable to other methods for acquiring field dynamics.²⁸ Consistent delays were determined for different slices, which suggests that the delay only needs to be calculated once at the beginning of the reconstruction pipeline for a single sample slice. This single-joint fit for τ and x can be performed with strong coil compression because this was shown to result in little error in τ . However, the image obtained from this joint fit of x and τ in the sample slice could have artifacts from coil compression (see Supporting Information Figure S2), and should therefore be discarded before reconstructing all slices via Equation 6 with the automatically determined τ and a more conservative choice of virtual coils. For our GPU implementation, the total time for determination of τ via Algorithm 1 was 14 s for spiral and 22 s for EPI when using 10 virtual coils and $\gamma_0 = 3$ (most time was spent on image formation via Equation 6). The longer time for EPI is due to additional k-space samples as well as additional iterations (Figure 3). The need for additional iterations likely stems from delays causing more substantial image artifacts for EPI (Figure 2), which leads to a poor estimate for the image in early iterations.

The proposed approach was proven to be effective for both single-shot spiral and EPI trajectories. When only six virtual channels are used, the accuracy in τ for the spiral case is slightly lower than for the EPI case (Figure 4), which likely occurs because an error in the delay only causes very subtle artifacts for spiral trajectories that may be difficult for the algorithm to detect in the presence of noise (eg, Figure 2).

When the initial guess for the delay is far from the true value, several starting guesses for τ may be required to find the global minimum, as Algorithm 1 is not globally convex (eg, for EPI as in Figure 4B); that said, the sub-problems defined by Equations 5 and 6 are each convex. However, for all scans used on our system so far (resolutions of 1.1 mm to 2 mm, accelerations by factors of 2–5), the initial guess has been within approximately $1 \mu\text{s}$ from the optimum value determined from Algorithm 1 for both EPI and spiral.

In other tests, we found that this method fails when only a single receiver channel is used (data not shown). Accordingly, the ability to estimate τ likely stems from consistency between the data and receiver sensitivity profiles (ie, C^j in Equation 1). The nature of this approach can be intuitively understood by considering the effect of synchronization delays on the solution of Equation 6. For single-shot spiral, a delay primarily causes blurring and a slight rotation of the multichannel image data relative to the coil sensitivities, which increases the residual

in the loss function $\|A_p x - Y\|_2^2$; accordingly, an optimal choice of τ from Equation 5 will minimize this inconsistency. Other trajectories would have similar effects. For example, a timing delay for EPI creates ghosting²⁹ and for a radial acquisition creates streaking artifacts,¹⁵ which are both inconsistent with the sensitivity profiles. Moreover, because other less-general approaches enforcing self-consistency have been effective for radial trajectories,¹⁵ it is likely that Algorithm 1, which is also based on self-consistency, would also be successful for this and likely other trajectories. Notably, the algorithm would not be successful for trajectories in which delays only cause a benign phase ramp in the object domain (eg, basic multishot Cartesian trajectories), because there would be no inconsistency with the receiver sensitivities created by the delay error; however, there is also likely little need to accurately determine the synchronization delay in these cases because the delay would not cause any harmful artifacts.

There are two user-defined parameters for this algorithm: the number of virtual coils and the convergence acceleration parameter γ . Even though we saw minimal image artifacts even when using as low as six virtual coils (Supporting Information Figure S2), the large increase in error in τ when moving from 10 to 6 coils (Figure 4) suggests that there may be individual cases in which image artifacts are encountered. Accordingly, we recommend a somewhat conservative choice of coils for all cases, such as 8 to 12 virtual coils for a 32-channel receiver. Also, while a suboptimal choice of γ lengthens the time for convergence, it has no impact on the accuracy aside from the unlikely event that it is so large that it brings the delay to a basin of attraction for a local minimum.

While Algorithm 1 only considers a single synchronization delay, it could easily be adapted to estimate different delays on the different gradient channels (ie, τ becomes a vector in Equation 5). This adaptation of the algorithm would be appropriate for acquisitions that do not use field monitoring. However, for these cases it would likely be preferred to account for the relative delays between channels and other trajectory errors from eddy currents via a gradient impulse response function.⁴ Notably, it is possible that there may still exist a global synchronization delay error even after correction with a gradient impulse response function, and, accordingly, Algorithm 1 may be applicable for such situations as well. Finally, Algorithm 1 could likely be extended to multishot sequences (notably, the synchronization delay is not expected to vary with shots); however, echo-time shifting such as that used for interleaved EPI would need to be accounted for.

6 | CONCLUSIONS

This work introduced a new model-based retrospective approach to automatically determine the synchronization delay between field dynamics and MRI data, which obviates the need for pulse sequence modifications or manual tuning to determine delays.

FUNDING INFORMATION

The Natural Sciences and Engineering Research Council of Canada (NSERC; RGPIN-2018-05448), Canada First Research Excellence Fund to BrainsCAN, Ontario Graduate Scholarship program, Canada Foundation for Innovation and the NSERC PGS-D program

DATA AVAILABILITY STATEMENT

The source code used for the expanded encoding model reconstructions is publicly available at <https://gitlab.com/cfmm/matlab/matmri>.³⁰ A demo for Algorithm 1 is included.

ORCID

Corey Allan Baron  <https://orcid.org/0000-0001-7343-5580>

TWITTER

Corey Allan Baron  @cabaron31

REFERENCES

- Mason GF, Harshbarger T, Hetherington HP, Zhang Y, Pohost GM, Twieg DB. A method to measure arbitrary k-space trajectories for rapid MR imaging. *Magn Reson Med*. 1997;38:492-496.
- Duyn JH, Yang Y, Frank JA, van der Veen JW. Simple correction method for k-space trajectory deviations in MRI. *J Magn Reson*. 1998;132:150-153.
- Zhang Y, Hetherington HP, Stokely EM, Mason GF, Twieg DB. A novel k-space trajectory measurement technique. *Magn Reson Med*. 1998;39:999-1004.
- Addy NO, Wu HH, Nishimura DG. Simple method for MR gradient system characterization and k-space trajectory estimation. *Magn Reson Med*. 2012;68:120-129.
- Vannesjo SJ, Haerberlin M, Kasper L, et al. Gradient system characterization by impulse response measurements with a dynamic field camera. *Magn Reson Med*. 2013;69:583-593.
- Ianni JD, Grissom WA. Trajectory auto-corrected image reconstruction. *Magn Reson Med*. 2016;76:757-768.
- Wilm BJ, Barmet C, Pavan M, Pruessmann KP. Higher order reconstruction for MRI in the presence of spatiotemporal field perturbations. *Magn Reson Med*. 2011;65:1690-1701.
- De Zanche N, Barmet C, Nordmeyer-Massner JA, Pruessmann KP. NMR probes for measuring magnetic fields and field dynamics in MR systems. *Magn Reson Med*. 2008;60:176-186.

9. Wilm BJ, Barmet C, Gross S, et al. Single-shot spiral imaging enabled by an expanded encoding model: demonstration in diffusion MRI. *Magn Reson Med.* 2017;77:83-91.
10. Kasper L, Bollmann S, Vannesjo SJ, et al. Monitoring, analysis, and correction of magnetic field fluctuations in echo planar imaging time series. *Magn Reson Med.* 2015;74:396-409.
11. Robison RK, Devaraj A, Pipe JG. Fast, simple gradient delay estimation for spiral MRI. *Magn Reson Med.* 2010;63:1683-1690.
12. Peters DC, Derbyshire JA, McVeigh ER. Centering the projection reconstruction trajectory: reducing gradient delay errors. *Magn Reson Med.* 2003;50:1-6.
13. Jung Y, Jashnani Y, Kijowski R, Block WF. Consistent non-cartesian off-axis MRI quality: calibrating and removing multiple sources of demodulation phase errors. *Magn Reson Med.* 2007;57:206-212.
14. Wech T, Tran-Gia J, Bley TA, Köstler H. Using self-consistency for an iterative trajectory adjustment (SCITA). *Magn Reson Med.* 2015;73:1151-1157.
15. Deshmane A, Blaimer M, Breuer F, et al. Self-calibrated trajectory estimation and signal correction method for robust radial imaging using GRAPPA operator gridding. *Magn Reson Med.* 2016;75:883-896.
16. Lobos RA, Kim TH, Hoge WS, Haldar JP. Navigator-free EPI ghost correction with structured low-rank matrix models: new theory and methods. *IEEE Trans Med Imaging.* 2018;37:2390-2402.
17. Bhavsar PS, Zwart NR, Pipe JG. Fast, variable system delay correction for spiral MRI. *Magn Reson Med.* 2014;71:773-782.
18. Jiang W, Larson PEZ, Lustig M. Simultaneous auto-calibration and gradient delays estimation (SAGE) in non-Cartesian parallel MRI using low-rank constraints. *Magn Reson Med.* 2018;80:2006-2016.
19. Akima H. A new method of interpolation and smooth curve fitting based on local procedures. *J ACM.* 1970;17:589-602.
20. Buehrer M, Pruessmann KP, Boesiger P, Kozerke S. Array compression for MRI with large coil arrays. *Magn Reson Med.* 2007;57:1131-1139.
21. Huang F, Vijayakumar S, Li Y, Hertel S, Duensing GR. A software channel compression technique for faster reconstruction with many channels. *Magn Reson Imaging.* 2008;26:133-141.
22. King SB, Varosi SM, Duensing GR. Optimum SNR data compression in hardware using an Eigencoil array. *Magn Reson Med.* 2010;63:1346-1356.
23. Zhang T, Pauly JM, Vasanawala SS, Lustig M. Coil compression for accelerated imaging with Cartesian sampling. *Magn Reson Med.* 2013;69:571-582.
24. Gilbert KM, Dubovan PI, Gati JS, Menon RS, Baron CA. Integration of an RF coil and commercial field camera for ultrahigh-field MRI. *Magn Reson Med.* 2022;87:2551-2565.
25. Larsson EG, Erdogmus D, Yan R, Principe JC, Fitzsimmons JR. SNR-optimality of sum-of-squares reconstruction for phased-array magnetic resonance imaging. *J Magn Reson.* 2003;163:121-123.
26. Uecker M, Lai P, Murphy MJ, et al. ESPIRiT—an eigenvalue approach to autocalibrating parallel MRI: where SENSE meets GRAPPA. *Magn Reson Med.* 2014;71:990-1001.
27. Baron CA, Dwork N, Pauly JM, Nishimura DG. Rapid compressed sensing reconstruction of 3D non-Cartesian MRI. *Magn Reson Med.* 2018;79:2685-2692.
28. Stärkind H, Boer VO, Jensen K, Polzik ES, Petersen ET. Optical field probes for MRI. *Proceedings of the 2020 ISMRM & SMRT Virtual Conference & Exhibition;* 2020:0653.
29. Bruder H, Fischer H, Reinfelder HE, Schmitt F. Image reconstruction for echo planar imaging with nonequidistant k-space sampling. *Magn Reson Med.* 1992;23:311-323.
30. Baron CA. MatMRI: a GPU enabled package for model based MRI image reconstruction. 2021. doi:10.5281/zenodo.5708265

SUPPORTING INFORMATION

Additional supporting information may be found in the online version of the article at the publisher's website.

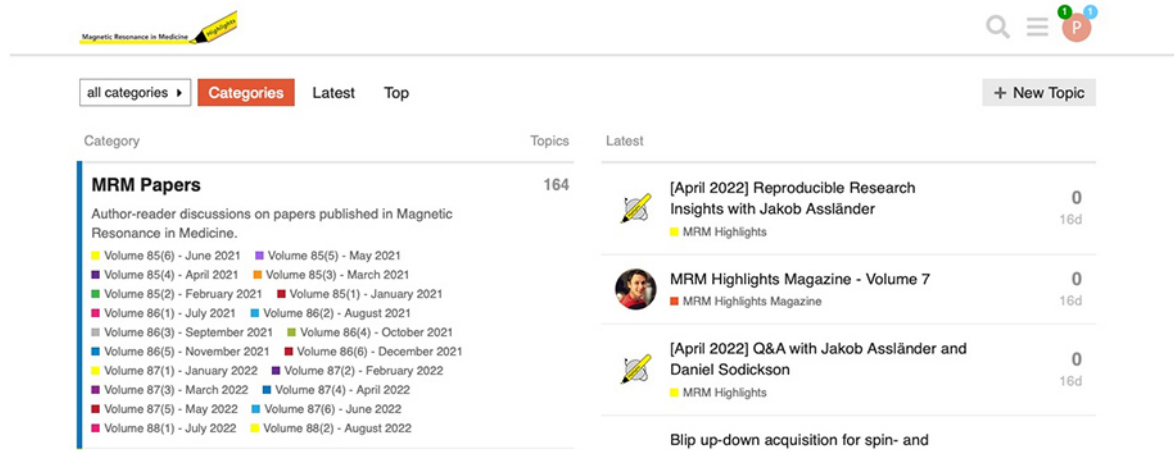
Figure S1. Simulation results for no noise (A), noise added (SNR ~ 10) for 1- μ s error in τ (B), and the result of using Algorithm 1 for noise added (SNR ~ 10) and an initial error in τ of 1 μ s (C). The right column for each read-out type shows the difference relative to the ground truth, scaled by a factor of 2. Simulated data, Y, was determined from Equation 1 using an image from the B_0 mapping scan as x . Mild artifacts are visible for spiral, whereas substantial artifacts are observed for EPI. $N_r = 32$ for all cases

Figure S2. Image reconstructions performed using in vivo data in a two-step process, where in step 1 the synchronization delay τ is determined via Algorithm 1 using $N_{r,\text{delay}}$ virtual coils, and then in step 2 that value of τ is used in Equation 6 with $N_{r,\text{image}}$ virtual coils to determine the final image. The right half of each image shows the difference from the reference image in the top row, scaled by a factor of 5. The error in τ is computed as the difference in τ relative to the case where all 32 coils were used for both steps. Although the solution to Equation 6 exhibits errors for a low number of virtual coils, Algorithm 1 produces relatively accurate estimations of τ for all cases. This suggests that the subproblem defined by Equation 5 (determination of τ) is better conditioned than the subproblem defined by Equation 6 (determination of the image), which is expected due to many orders of magnitude fewer unknown variables to solve for in the former case. Similar results are obtained in other slices

How to cite this article: Dubovan PI, Baron CA. Model-based determination of the synchronization delay between MRI and trajectory data. *Magn Reson Med.* 2022;1-8. doi: 10.1002/mrm.29460

WOULD YOU LIKE TO POST AN INFORMAL COMMENT ABOUT THIS PAPER, OR ASK THE AUTHORS A QUESTION ABOUT IT?

If so, please visit <https://mrm.ismrm.org/> and register for our Magn Reson Med Discourse site (registration is free).



The screenshot shows the Magn Reson Med Discourse website. At the top, there is a search bar and a navigation menu. Below the navigation, there are tabs for 'all categories', 'Categories', 'Latest', and 'Top'. A '+ New Topic' button is also visible. The main content area is divided into two columns: 'Category' and 'Topics'. The 'Category' column lists 'MRM Papers' with a description and a list of volumes from 85(6) to 88(2). The 'Topics' column shows a list of recent topics, including '[April 2022] Reproducible Research Insights with Jakob Assländer', 'MRM Highlights Magazine - Volume 7', and '[April 2022] Q&A with Jakob Assländer and Daniel Sodickson'. Each topic has a '0' comment count and a '16d' timestamp.

Magn Reson Med is currently listing the top 8 downloaded papers from each issue (including Editor's Picks) for comments and questions on the Discourse web site.

However, we are happy to list this or any other papers (please email mrm@ismrm.org to request the posting of any other papers.)

We encourage informal comment and discussion about Magn Reson Med papers on this site. Please note, however, that a formal errata from the authors should still be submitted in the usual way via our Manuscript Central online submission system.